inorganics

MDPI

Article

Precipitative Coating of Calcium Phosphate on Microporous Silica–Titania Hybrid Particles in Simulated Body Fluid

Reo Kimura [1], Kota Shiba [2,*], Kanata Fujiwara [1], Yanni Zhou [1], Iori Yamada [1,3] and Motohiro Tagaya [1,*]

[1] Department of Materials Science and Bioengineering Technology, Nagaoka University of Technology, Kamitomioka 1603-1, Nagaoka 940-2188, Japan
[2] Center for Functional Sensor & Actuator, Research Center for Functional Materials, National Institute for Materials Science (NIMS), 1-1, Namiki, Tsukuba 305-0044, Japan
[3] Research Fellow of the Japan Society for the Promotion of Science (DC), 5-3-1 Koji-machi, Chiyoda-ku, Tokyo 102-0083, Japan
* Correspondence: shiba.kota@nims.go.jp (K.S.); tagaya@mst.nagaokaut.ac.jp (M.T.)

Abstract: Titania and silica have been recognized as potential drug delivery system (DDS) carriers. For this application, controllable biocompatibility and the suppression of the initial burst are required, which can be provided by a calcium phosphate (CP) coating. However, it is difficult to control the morphology of a CP coating on the surface of carrier particles owing to the homogeneous nucleation of CP. In this study, we report the development of a CP-coating method that homogeneously corresponds to the shapes of silica–titania (SiTi) porous nanoparticles. We also demonstrate that controlled surface roughness of CP coatings could be achieved in SBF using SiTi nanoparticles with a well-defined spherical shape, a uniform size, and a tunable nanoporous structure. The precipitation of CP was performed on mono-dispersed porous SiTi nanoparticles with different Si/Ti molar ratios and pore sizes. The pore size distribution was found to significantly affect the CP coating in SBF immersion; the surfaces of the nanoparticles with bimodal pore sizes of 0.7 and 1.1–1.2 nm became rough after CP precipitation, while those with a unimodal pore size of 0.7 nm remained smooth, indicating that these two pore sizes serve as different nucleation sites that lead to different surface morphologies.

Keywords: bioceramic nanoparticles; simulated body fluid; nanopore; CP precipitative coating; silica–titania nanohybrid

Citation: Kimura, R.; Shiba, K.; Fujiwara, K.; Zhou, Y.; Yamada, I.; Tagaya, M. Precipitative Coating of Calcium Phosphate on Microporous Silica–Titania Hybrid Particles in Simulated Body Fluid. *Inorganics* **2023**, *11*, 235. https://doi.org/10.3390/inorganics11060235

Academic Editors: Roberto Nisticò and Silvia Mostoni

Received: 11 April 2023
Revised: 23 May 2023
Accepted: 24 May 2023
Published: 28 May 2023

1. Introduction

Various nanomaterials composed of bioinert ceramics have been synthesized for use as artificial joints, implants, and drug delivery system (DDS) carriers [1,2]. In these applications, a DDS carrier needs to fulfill many requisites, including not only the inherent biocompatibility of bioceramic-based materials but also other properties including being of a uniform shape, size, and size distribution and possessing high affinity for aqueous media in order to form a stable suspension [3–5]. A sol–gel method based on the hydrolysis and condensation of a metal alkoxide has been used to synthesize a variety of biocompatible metal oxide nanoparticles with controlled morphologies, for which titania and silica have been extensively studied [6–8]. For example, amorphous titania in nanotube form has been investigated with respect to its use as a DDS carrier [9,10]. Since the surface of titania exhibits a Zeta potential of −18 mV [11] in water (at pH 7.4), serious aggregate formation can occur depending on the experimental conditions. By contrast, amorphous silica shows a higher Zeta potential of −60 mV in water (at pH 7.4) [12], allowing for the formation of a relatively stable suspension [13,14]. Although mixed oxide nanoparticles composed of silica and titania (SiTi nanoparticles) [15] have been explored as another potential option, their use also poses the problems such as biotoxicity due to the release of a silicate ion elusion into the biological solution [16] and difficulty in controlling drug release owing to

the initial burst [17,18]. Therefore, the surfaces of SiTi nanoparticles need to be properly designed before being used for DDS applications.

Calcium phosphate (CP) coating has been developed as a technique to improve the osteoconductivity of the surfaces of titanium implants [19–21]. The CP coating is thought to suppress the initial burst of drug molecules [22], allowing them to be released gradually over several weeks. This is due to the fact that the CP coating itself can act as a reservoir for drug molecules, which slowly dissolve and diffuse over time as the coating degrades. The general CP-coating methods are electrochemical deposition, sputtering, and plasma spraying, which are performed under unphysiological conditions such as at high temperatures to provide different chemical and crystalline states with respect to the bone hydroxyapatite [23–25], leading to lower bioactivity in vivo. The biomimetic method has attracted attention due to its potential benefits. In this approach, CP is precipitated on particles in simulated body fluid (SBF) under conditions that mimic the biological environment of a living body [26,27]. Biomimetic CP synthesized under these conditions has been found to be more bioactive than CP synthesized under higher-temperature conditions [28–30]. However, biomimetic CP has generally only been coated on flat substrates [31–35]. In the case of nanoparticles, uniform nucleation occurs at different positions from the particle surfaces due to their high curvature and lower ability to induce heterogeneous nucleation. Therefore, a coating technique that adapts to the shapes of nanoparticles and provides a uniform coating has not been developed.

In this study, we demonstrate that controlled surface roughness of CP coatings can be achieved in SBF by using SiTi nanoparticles with a well-defined spherical shape, a uniform size, and a tunable nanoporous structure (Scheme 1). We synthesized SiTi nanoparticles using a microfluidic approach [15], which allowed us to design their size and shape so that they were suitable for DDS, and used them as a scaffold for the CP coating. The SiTi nanoparticles serve two critical functions in the SBF: they (1) provide CP nucleation sites that promote the substitution of phosphate ions with silicate ions and (2) create nanopores that induce the selective adsorption of hydrated ions in SBF. As described, the silicate ions elute readily into biological fluids [36,37] and can be replaced by phosphate ions [38], facilitating Ca^{2+} ion adsorption and subsequent CP nucleation. Moreover, the hydrated ions in SBF, including Na^{+}, K^{+}, and Ca^{2+}, can be adsorbed into the nanopores in their hydrated states and their sizes differ from each other. We prove that SiTi nanoparticles with tunable nanostructures can effectively function as an ion (molecular) sieve [39,40] that enables the selective adsorption of Ca^{2+} from SBF, leading to the formation of CP coatings. We also discuss the effect of nanopore sizes on the surface roughness of CP coatings.

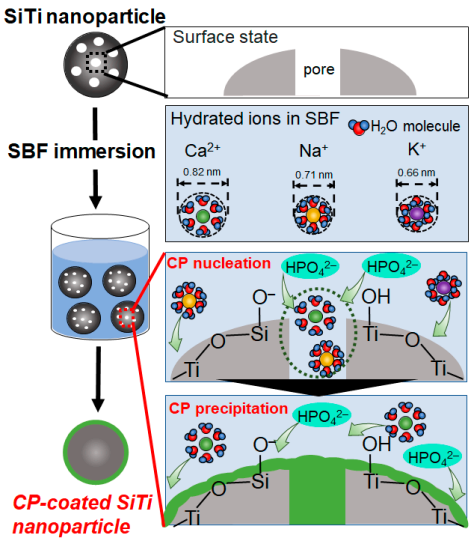

Scheme 1. Illustration of the CP precipitation process of the SiTi nanoparticles via immersion in SBF.

2. Results and Discussion

2.1. Synthesis Result of XSiTi Nanoparticles

The Si/Ti molar ratios were measured via XRF and the values were X, and the sample was named as XSiTi (X = 0, 0.1, 0.7, and 1.2). The FE-SEM images and size distributions of the XSiTi nanoparticles are shown in Figure 1. All the SiTi nanoparticles exhibited spherical and mono-dispersed states. The diameter of the particles was around 150–200 nm, which is considered a size that does not induce cytotoxicity [41,42].

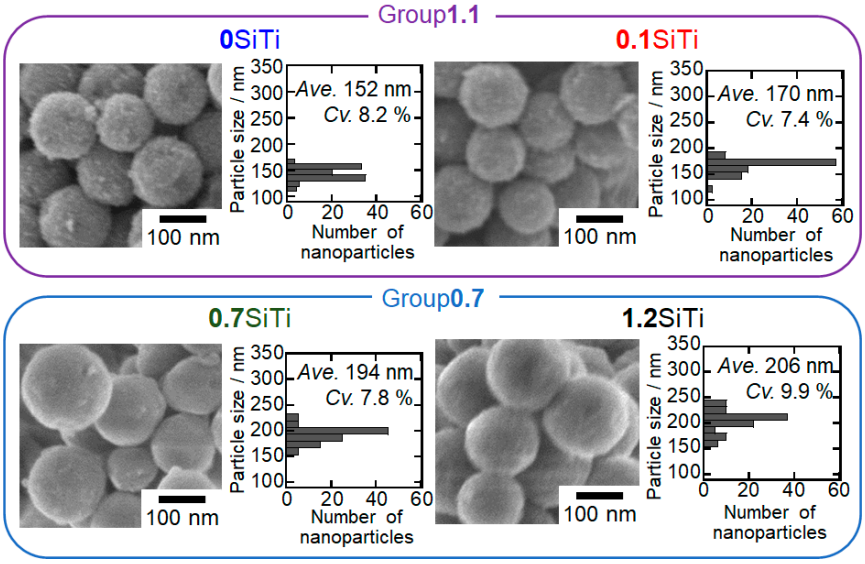

Figure 1. FE-SEM images and particle size distributions of the SiTi nanoparticles.

The XRD patterns (Figure S1) of the XSiTi nanoparticles indicated that all the nanoparticles were amorphous. Comparing the properties of these particles (e.g., particle shape, particle size, and CV value) with those of previously reported particles [15], we confirmed that they were identical and that equivalent particles were synthesized.

Figure 2 shows the N_2 adsorption and desorption isotherms of the SiTi nanoparticles. In the results regarding the specific surface area calculated using the αs-plot (Figure 2a), it is evident that the surface area increased with the increase in the Si/Ti molar ratio. According to the nanopore size distributions based on the MP (micropore) method in the results regarding the *X*SiTi nanoparticles (Figure 2b,d), 0SiTi and 0.1SiTi exhibited bimodal nanopore sizes of 0.7 and 1.1~1.2 nm, and 0.7SiTi and 1.2SiTi exhibited only monomodal pores of 0.7 nm. The different nanopore sizes occurred due to the increase in the Si/Ti molar ratio. We propose that the hydrated ions of SBF were potentially diffused and adsorbed into the nanopores (Figure 2c,e). We suggest that nanopores 0SiTi and 0.1SiTi, with pore sizes of 1.1~1.2 nm, enable the diffusion and adsorption of the hydrated Ca^{2+}, Na^+, and K^+ ions, while 0.7SiTi and 1.2SiTi, with a pore size of 0.7 nm, only allows for the diffusion and adsorption of the hydrated Na^+ and K^+ ions. According to the nanopore size distribution, 0SiTi and 0.1SiTi were defined as Group**1.1**, while 0.7SiTi and 1.2SiTi were defined as Group**0.7**. By comparing these nanopore diameters with those of previously reported particles [15], we confirmed that they are identical and that comparable particles had been synthesized.

2.2. Results Regarding the SBF-Immersed SiTi Nanoparticles

The chemical element (Ca, Na, and K) amounts adsorbed by the SiTi nanoparticles through immersion in SBF were evaluated via XRF (Figure 3). The adsorbed elements increased with an increased immersion time. Referring to the results regarding the change in the amount of Ca on the nanoparticles (Figure 3a), the amount in Group**1.1** was clearly larger than that in Group**0.7** at the initial stage, indicating that Ca was preferentially

adsorbed on the nanoparticles in Group**1.1**. By observing the amount changes of Na and K adsorbed on the nanoparticles (Figure 3b,c), it is evident that those of Group**0.7** were significantly larger than those in Group**1.1** at the initial stage, indicating that Na and K were preferentially adsorbed on the nanoparticles in Group**0.7**. These differences are thought to be due to the difference in the nanopore sizes between Group**1.1** and Group**0.7**. The diameters of the hydrated ions that could diffuse and be adsorbed inside the nanopores were determined as shown in Figure 2. The adsorption of Ca in Group**1.1** reached equilibrium within 1 day of immersion, while the other ions in Group**0.7** did not reach equilibrium even after 3 days. In addition, most of the adsorption of Na and K for Group**0.7** reached equilibrium within 1 day of immersion, whereas that for Group**1.1** did not reach equilibrium until 3 days.

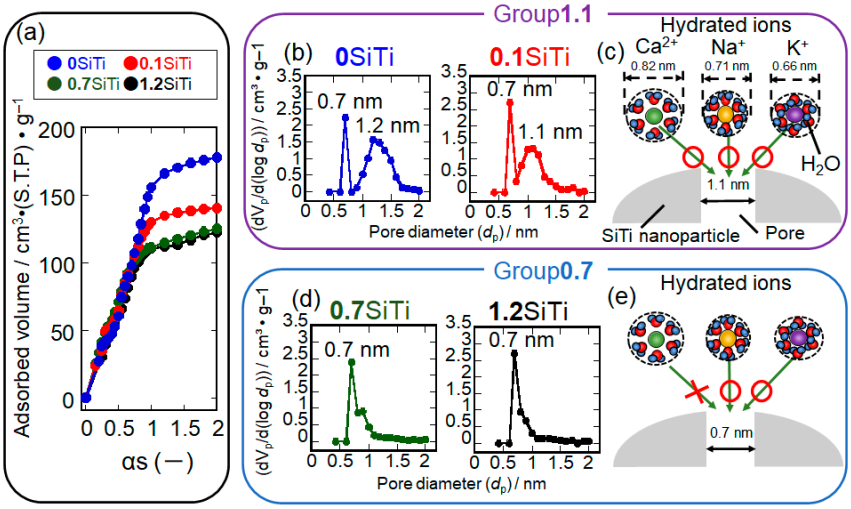

Figure 2. (**a**) N_2 adsorption (●) and desorption (○) isotherms of the SiTi nanoparticles; (**b**,**d**) the MP pore size distributions; and (**c**,**e**) illustrations of the hydrated ion interactions with the micropores. The specific surface areas of 0SiTi, 0.1SiTi, 0.7SiTi, and 1.2SiTi were 382, 443, 466, and 570 $m^2 \cdot g^{-1}$, respectively.

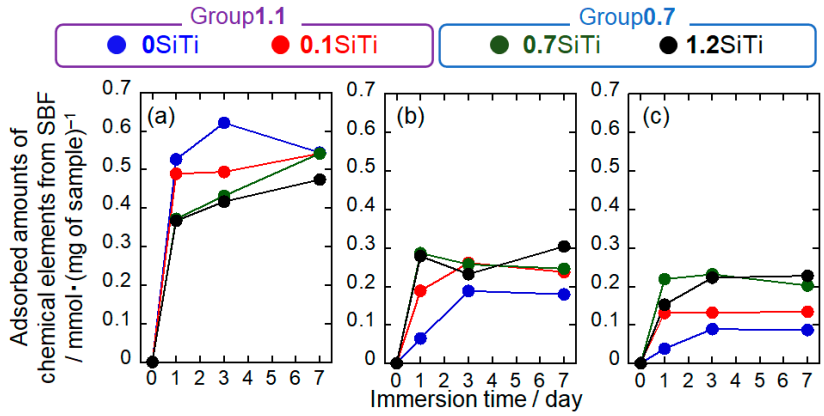

Figure 3. Adsorbed amount changes of the chemical elements of (**a**) Ca, (**b**) Na, and (**c**) K on the SiTi nanoparticles from SBF with immersion time.

The nucleation sites pertaining to the CP precipitation of SiTi nanoparticles immersed in SBF are discussed in Figure 4. Figure 4a shows the FT-IR spectra of the change in the absorbance band due to the OH group of the nanoparticles. The band intensity of Group**1.1** did not change after immersion, whereas Group**0.7** showed an increase in band intensity. The result of the change in the Si/Ti molar ratio of the nanoparticles after immersion is shown in Figure 4b. Group**1.1** did not change in terms of its Si/Ti molar ratio, whereas Group**0.7** showed a significant decrease, suggesting that the Si component was

eluted from Group0.7 into SBF. Regarding the changes in the average particle sizes of the nanoparticles following immersion (Figure 4c), all the nanoparticles showed a decrease in the size, and a significant decrease was observed in Group**0.7**. Group**1.1** containing lower Si-content did not show a change, while Group**0.7** with higher Si-content showed a change, indicating that the Si component's elution can induce CP precipitation. The mechanism behind the CP nucleation in the precipitation on Group**0.7** is suggested in Figure 4d. Group**0.7** preferentially absorbed the hydrated Na^+ and K^+ ions inside the nanopores. The Si-components in Group**0.7** were eluted as the silicate ions outside the nanopores, and the phosphate ions interacting with the H_2O component in SBF were adsorbed into the eluted sites [38]. The intensity of the OH group of Group**0.7** increased through immersion in SBF due to the subsequent adsorption of the hydrated Ca^{2+} ions and the consequent promotion of CP nucleation. Therefore, the outside nanopore surfaces are considered the CP nucleation sites for Group**0.7**.

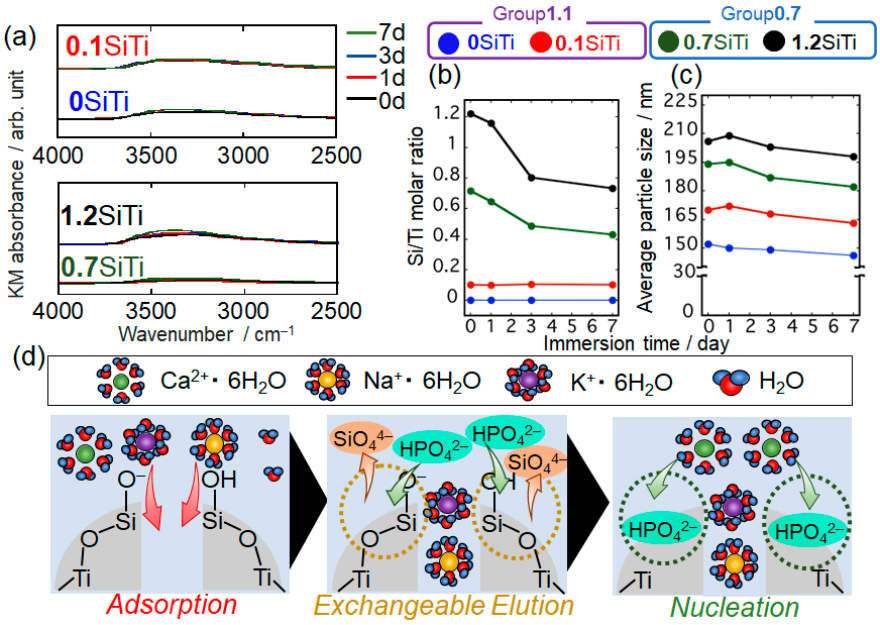

Figure 4. (**a**) FT-IR spectra, (**b**) Si/Ti molar ratio, and (**c**) average particle size changes of the SiTi nanoparticles with immersion time in SBF, and (**d**) illustrations of the possible interfacial reactions of Group**0.7** with the ions in SBF. Xd represents the immersion time of X days (X = 0, 1, 3, and 7).

In Figure 5, the characteristics of phosphate ion adsorption for the CP nucleation sites on Group**1.1** and Group**0.7** are evaluated and discussed. According to the changes of the absorption band generated by phosphate ions after immersion (Figure 5a), Group**1.1** and Group**0.7** showed increases in the absorbance bands of the stretching vibrations due to Ti–P–O [43], P–O, and P–OH bonds [44] at 1100, 1039–997, and 866–842 cm^{-1} following immersion. For Group**0.7**, the bands produced by Si–O–Si [45] and Si–OH [46] at 1039–997 and 866–842 cm^{-1} were also included in the spectra, and the shapes were different from those of Group**1.1**. The amount changes in the adsorbed phosphorous components of Group**1.1** and Group**0.7** showed an increase in the amount after immersion (Figure 5b). In particular, Group**1.1** reached the adsorption equilibrium after approximately 1 day of immersion, whereas Group**0.7** showed a slower adsorption rate, suggesting that the CP precipitate emerged at a relatively earlier stage in Group**1.1** compared to that of Group**0.7**. Figure 5c shows the possible illustrations of the nucleation sites of Group**1.1** and Group**0.7**. In Group**1.1**, the hydrated Ca^{2+} ions in addition to the Na^+ and K^+ ions were preferentially diffused and absorbed inside the nanopores, which serve as sites for CP nucleation. In Group**0.7**, the hydrated Na^+ and K^+ ions were preferentially diffused and absorbed inside the nanopores, and the phosphate ions were replaced with the sites where the silicate ions were eluted, suggesting that the outside of the nanopores serve as CP nucleation sites.

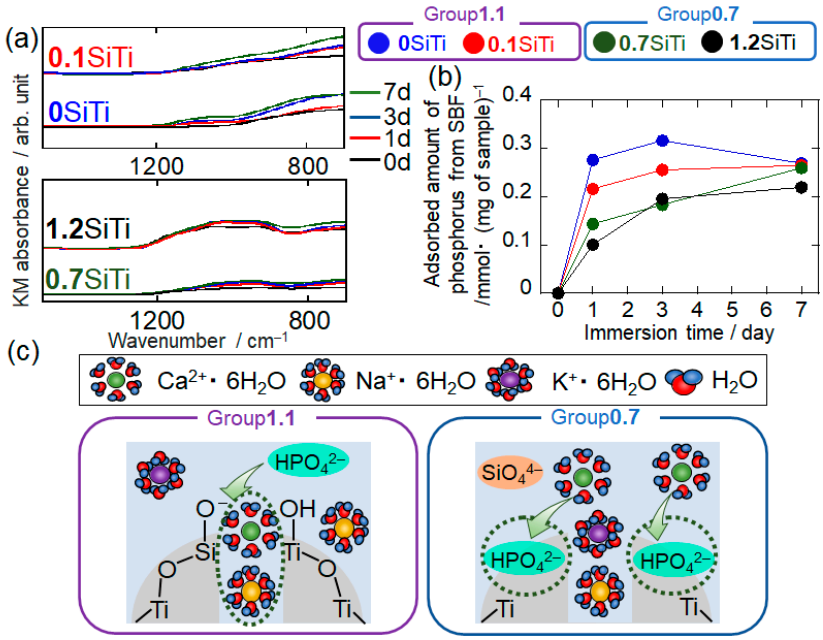

Figure 5. (**a**) FT-IR spectral changes of the SiTi nanoparticles with immersion time in SBF and (**b**) the adsorbed amount changes of phosphorus from SBF. (**c**) Illustrations of the possible calcium phosphate nucleation processes of Group**1.1** and Group**0.7**.

According to the FE-SEM images and particle size distributions of the SiTi nanoparticles (Figure 6), even after immersion for 7 days, the particles still exhibited spherical shapes and mono-dispersed states, indicating a preserved particle size of approximately 150–200 nm. In particular, Group**1.1** exhibited rough surfaces, whereas Group**0.7** retained smooth surfaces. These results show that CP was roughly precipitated on Group**1.1** but was smoothly precipitated on Group**0.7**, indicating that a smooth CP coating was achieved using Group**0.7**.

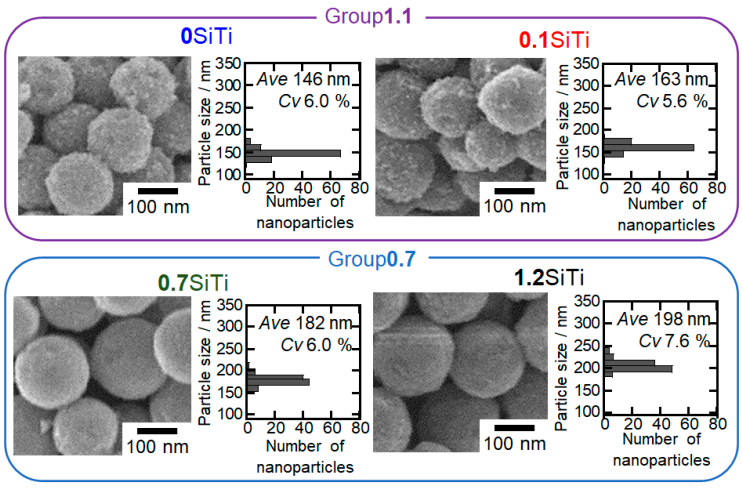

Figure 6. FE-SEM images and particle size distributions of the SiTi nanoparticles after immersion in SBF for 7 days.

The elemental mapping results and TEM images of 0.1SiTi and 1.2SiTi after their immersion are shown in Figure 7. The particle images (i.e., BF: STEM HAADF images) and shapes (i.e., locations) of the chemical elements were similar between Group**1.1** and Group**0.7** (Figure 7a,d), indicating that a homogeneous CP precipitation on the surfaces could be achieved by immersing the nanoparticles in SBF. The Ca signal for 0.1SiTi (Group**1.1**) was weaker than that for 1.2SiTi (Group**0.7**), which is possibly due to the different CP nucleation

mechanisms between Group**1.1** and Group**0.7** (as shown in Figure 5c). In Group**1.1**, the hydrated Ca^{2+} ions in addition to the Na^{+} and K^{+} ions were preferentially diffused and adsorbed inside the nanopores, which served as CP nucleation sites. The results suggested that the number of nucleation sites in Group**1.1** is smaller than that in Group**0.7**, indicating a lower amount of the CP precipitation. The contrast of 0.1SiTi (Group**1.1**) was different from that of 1.2SiTi (Group**0.7**), indicating the presence of rough surfaces due to the CP precipitation of Group**1.1** (Figure 7b,c,e,f).

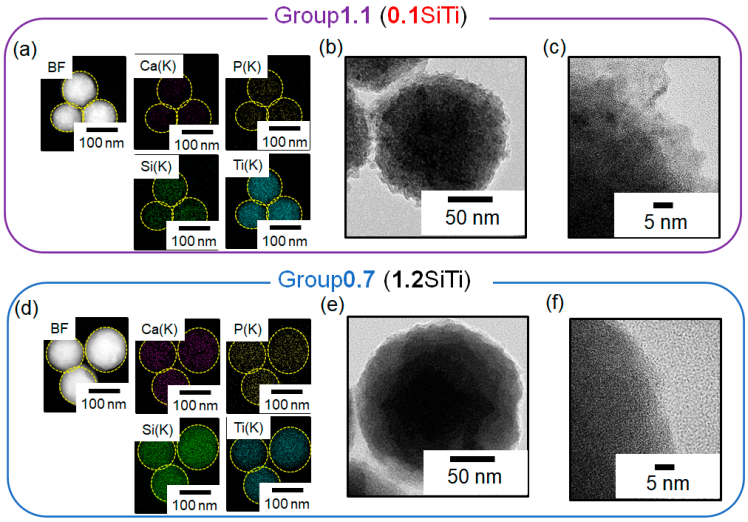

Figure 7. (**a**,**d**) STEM and EDS elemental mapping (Ca, P, Si, and Ti) images of the SiTi nanoparticles after immersion in SBF for 7 days. The detected energies for Ca(K), P(K), Si(K), and Ti(K) were 3.69, 2.01, 1.74, and 4.52 keV, respectively. The dotted yellow circles indicate areas where chemical elements are present. (**b**,**c**,**e**,**f**) TEM images of the SiTi nanoparticles after immersion in SBF for 7days.

The αs plots of the SiTi nanoparticles after immersion in SBF are shown in Figure S2. The changes in the specific surface area of the nanoparticles, which were determined based on the aforementioned results, are shown in Figure 8. Group**1.1** and Group**0.7** showed a decrease in the specific surface area following immersion, indicating the adsorption of the ions inside the nanopores. In particular, Group**1.1** showed a faster rate of decrease in surface area compared with Group**0.7** since nitrogen (N_2) molecules could not enter the nanopores where CP had effectively precipitated inside. Based on Figure 8, it can be observed that Group**1.1** presents a higher rate of reduction in external surface area determined from the αs-plot, indicating that the effective precipitation of CP was due to pore blockage. As a result, Group**1.1** exhibits a higher concentration of adsorbed phosphorous (i.e., phosphate ions). The lower reduction in the specific surface area in Group**0.7** suggests lesser pore blockage through calcium ion adsorption. Since the slight reduction in the surface area is attributed to Na^{+} and K^{+} ions, it can be inferred that this reduction in surface area is less significant in the present paper. Therefore, the distribution of pores in Group **1.1** is considered a random array shape. Moreover, the peaks of Group**1.1** with bimodal distributions decreased after immersion (Figure S3). The nanopores of 0SiTi at 1.2 nm decreased to 1.0 nm, while the nanopores of 0.1SiTi at 1.1 nm decreased to 0.9 nm. Figure S4 shows the N_2 adsorption and desorption isotherms during immersion. According to a previous report [47], the isotherm type of Group**1.1** was type IV before immersion, which changed to type I after immersion. The isotherm of Group**0.7** remained type I after SBF immersion, indicating that the nanopore structures in Group**1.1** were preserved upon their immersion. Regarding pore size distribution, Group**1.1** shows bimodal shapes in Figure S3. It was suggested that pore blockage in the 1.1 nm sized particles of Group**1.1** would occur, whereas the pores at 0.7 nm remained unblocked, thereby maintaining microporous structures. After immersion, the adsorption isotherm of Group**1.1** in SBF was changed such that is similar in shape to that of Group**0.7** (Figure S4).

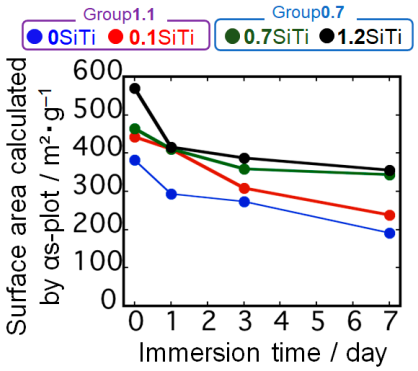

Figure 8. Specific surface area changes of the SiTi nanoparticles with immersion time in SBF. The reduction percentages in the surface areas of 0SiTi, 0.1SiTi, 0.7SiTi, and 1.2SiTi were 50, 46, 26, and 38%.

Accoring to the XRD pattern results, after their immersion in SBF for 14 days, Group**1.1** and Group**0.7** remained amorphous (Figure S5). All of the nanoparticles showed an amorphous calcium phosphate (ACP) halo peak at 2θ = 30°, indicating the precipitation of ACP on their surfaces.

2.3. Mechanism of ACP Precipitation on XSiTi Nanoparticles after Immersion

Based on the above results and discussion, the mechanisms of ACP precipitation in Group**1.1** and Group**0.7** are shown in Scheme 2. Regarding Group**1.1**, the Ca^{2+} ions were diffused and adsorbed inside the nanopores after immersion within one day. The Ca^{2+} ions inside the nanopores reacted with the phosphate ions in SBF, and the nanopores became the ACP nucleation sites, leading to rough ACP precipitation. For Group**0.7**, only the Na^+ and K^+ ions were diffused and adsorbed inside the nanopores after immersion for one day. The phosphate ions exchanged with the eluted silicate ions outside the nanopores and became the ACP nucleation sites. Therefore, it was determined that the ACP precipitation state was smooth without changing the surface morphology of Group**0.7**.

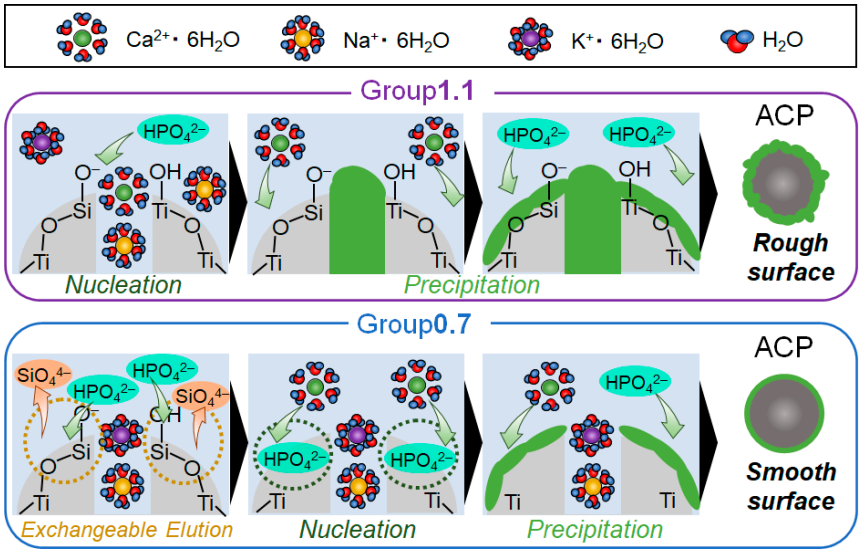

Scheme 2. Illustration of the precipitation processes of the SiTi nanoparticles in this study.

3. Materials and Methods

3.1. Chemicals

TEOS ($C_8H_{20}O_4Si$: CAS No. 78-10-4) and TTIP ($C_{12}H_{28}O_4Ti$: CAS No. 546-68-9) were purchased from Tokyo Chemical Industry Co., Ltd. 2-Propanol (IPA, CAS No.

67-63-0), hydrochloric acid (HCl, 1 N, CAS No. 7647-01-0), ethanol (EtOH, 99.5 vol %, CAS No. 64-17-5), tris-hydroxymethylaminomethane (Tris, $C_4H_{11}NO_3$, CAS No. 77-86-1), sodium chloride (NaCl, CAS No. 7647-14-5), potassium chloride (KCl, CAS No. 7447-40-7), dipotassium hydrogenphosphate (K_2HPO_4, CAS No. 7758-11-4), magnesium chloride hexahydrate ($MgCl_2 \cdot 6H_2O$, CAS No. 7791-18-6), calcium chloride ($CaCl_2$, CAS No. 10043-52-4), and sodium sulfate (Na_2SO_4, CAS No. 7757-82-6) were purchased from FUJIFILM Wako Pure Chemical Co., Ltd. Sodium hydrogen carbonate ($NaHCO_3$, CAS No. 144-55-8) was purchased from Nacalai Tesque Co., Ltd. Octadecylamine (ODA, $CH_3(CH_2)_{17}NH_2$, CAS No. 124-30-1) was purchased from Sigma Aldrich Co., Ltd. All reagents are unpurified.

3.2. Synthesis

3.2.1. Synthesis of SiTi Nanoparticles

In a previous report [15], SiTi nanoparticles were synthesized via microfluidic synthesis. Initially, three solutions (A–C) were prepared. Volumes of 1.63 mL of TTIP and 0, 0.187, 1.705, and 15.34 mL of TEOS were added to solution A to form Si/Ti molar ratios of 0, 0.15, 1.4, and 12, respectively, and 43.30, 43.11, 41.60, and 27.96 mL volumes of IPA were added according to the ratios. Solution B was prepared by mixing 44.60 mL of IPA and 0.277 mL of ultrapure water. Solution C was prepared by mixing 236.1 mL of IPA, 3.00 mL of ultrapure water, and 0.205 g of ODA. Solutions A and B were then mixed and reacted in a microreactor to generate nucleation via a sol–gel process, and the reaction solution was dropped into Solution C at a flow rate of 60 mL/min at 1000 rpm and left to grow the particles for 24 h under the room temperature. The liquid portion was removed via centrifugation, washed with ethanol and ultrapure water, and then dried at 60 °C for 24 h to obtain the SiTi nanoparticles with ODA (SiTi-ODA). Next, 10.2 mL of 1 N HCl and 150 mL of ethanol were added into 1 g of the dried SiTi-ODA, and the mixture was stirred at 700 rpm for 3 h at room temperature to remove ODA through solvent extraction. The solid phase was then removed via centrifugation and washed once with ethanol and once with ultrapure water. The particles were dried at 60 °C for 24 h to obtain nanoporous SiTi nanoparticles.

3.2.2. Immersion of SiTi Nanoparticles into SBF

The 1.0 SBF (Na^+, 142 mM; K^+, 5.0 mM; Mg^{2+}, 1.5 mM; Ca^{2+}, 2.5 mM; Cl^-, 148.8 mM; HCO_3^-, 4.2 mM; HPO_4^{2-}, 1.0 mM; SO_4^{2-}, 0.5 mM; and Tris, 50 mM) was prepared according to the method provided in a previous report [48], and the pH value was adjusted to 7.4 with HCl. Then, 0.5 SBF and 1.5 SBF were prepared at 0.5 and 1.5 times the inorganic ion concentrations of 1.0 SBF. After the XSiTi nanoparticles were added to 0.5 SBF, the pH value was adjusted to 8.60 with Tris and kept at 37 °C for 1 day. The particles were then immersed in 1.5 SBF for 7 days. The solid phase was removed via centrifugation and dried at 37 °C for 24 h to obtain CP-coated SiTi nanoparticles.

3.3. Characterization

The morphologies were observed on a carbonblack-coated Cu grid using a field emission scanning electron microscope (FE-SEM: HITACHI Co., Ltd., SU-8230) at an accelerating voltage of 200 kV; the vertical size, side size, and particle size distributions of the SiTi nanoparticles' shapes were calculated by counting 150 particles, and their average (Ave.) and coefficient of variation (Cv.) values were also calculated. Size distributions of the SiTi nanoparticle images obtained through FE-SEM were calculated by randomly selecting 150 particles.

X-ray diffraction (XRD) patterns were obtained using a powder X-ray diffractometer (Rigaku Co., Ltd., Smart Lab) with CuKα radiation (λ = 0.15418 nm), a voltage of 40 kV, and a current of 200 mA.

Specific surface area and pore size distribution determined via N_2 adsorption and desorption isotherms were measured at −196 °C with a BELSORP-Mini II instrument

(Microtrac BEL Co., Ltd.) to estimate the total surface areas. Prior to measurement, 100 mg of each sample was degassed and pretreated at 80 °C under a vacuum. The following methods were used to analyze the nanopores. The specific surface area was evaluated using the αs-plots [49], and the pore size distribution was determined using micropore analysis (MP). Furthermore, *t*-plots were used to calculate the specific surface area inside the pores and the adsorbed layers' thickness [50,51]; then, the pore volume was obtained. In this study, the Harkins−Jula equation representing the standard *t*-curve was used to investigate the standard isotherm. This curve is one of the most commonly used MP methods. Pore size was defined as dp, which was plotted against dVp/dlog dp to show the pore size distribution.

Elemental composition was evaluated using an X-ray fluorescence analyzer (XRF: ZSX Primus II, Rigaku Co., Ltd.). XRF analysis was performed on sample powders in the state of pellets, which were pressurized and molded without dilution. The fundamental parameter method was conducted using software for semi-quantitative analysis (EZ Scan Program, Rigaku Co., Ltd.). Specifically, the amount of each element (Ca, Na, K, and P) adsorbed from SBF was detected and then evaluated in terms of mmol·(mg of sample)$^{-1}$ on a semi-quantitative basis.

Infrared absorption spectra were measured using a Fourier transform infrared spectrometer (FT-IR: FT/IR-4600, Japan Spectroscopic Co., Ltd.) operating in the wavenumber range 4000–500 cm^{-1} with a KBr background, 128 accumulation times, and a spectral resolution of 4 cm^{-1}. FT-IR spectra were measured using KBr powder, and all weights were determined with 49 mg of KBr and 1 mg of sample. All the spectra were recorded after subtracting the background spectrum of KBr.

Transmission electron microscopy (TEM) was performed using a JEOL JEM-2100F transmission electron microscope. Scanning TEM high-angle annular dark-field (STEM−HAADF) images and elemental mapping energy-dispersive X-ray (EDX) spectroscopy images were recorded using a JEM-2100F and a JED-2300 instrument (EX-24200M1G2T, JEOL Ltd.) at an accelerating voltage of 200 kV. The sample suspension was dropped onto a Cu grid (a high-resolution carbon substrate on STEM 100CuP grids, Okenshoji Co., Ltd.), and the grids were dried under vacuum for a few days before each measurement. STEM and EDS elemental mapping (Ca, P, Si, and Ti) images of the SiTi nanoparticles were taken after the nanoparticles' immersion in SBF for 7 days. The detected energies for Ca(K), P(K), Si(K), and Ti(K) were 3.69, 2.01, 1.74, and 4.52 keV, respectively.

4. Conclusions

We established a CP-coating method that homogeneously corresponds to the shapes of SiTi nanoparticles. CP precipitation was performed on mono-dispersed nanoporous SiTi nanoparticles with different Si/Ti molar ratios and pore sizes. The pore size distribution was found to significantly affect the CP coating in SBF immersion; the surfaces of the nanoparticles with bimodal pore sizes of 0.7 and 1.1~1.2 nm became rough after CP precipitation, while those with unimodal pore sizes of 0.7 nm remained smooth, indicating that these two pore sizes work as different nucleation sites that lead to different surface morphologies. These CP-coated SiTi nanoparticles could improve osteoconductivity while retaining the properties of SiTi nanoparticles, which we believe may be suitable for use in the DDS carriers in the future.

Supplementary Materials: The following supporting information can be downloaded at: https://www.mdpi.com/article/10.3390/inorganics11060235/s1, Scheme S1: XRD patterns of the SiTi nanoparticles.; Figure S2: αs-plots of the SiTi nanoparticles with the immersion time ***X***d (***X*** days, ***X***=0, 1, 3, 7) in SBF; Figure S3: The MP pore size distribution of SiTi nanoparticles with the immersion time in SBF; Figure S4: N_2 adsorption (close marks) and desorption (open marks) isotherms of the SiTi nanoparticles with the immersion time in SBF; Figure S5: XRD patterns of the SiTi nanoparticles at the immersion time in SBF for 14 days.

Author Contributions: Conceptualization, R.K. and M.T.; methodology, R.K., K.F. and M.T.; software, R.K.; validation, K.F. and M.T.; formal analysis, I.Y. and K.S.; investigation, R.K.; resources, M.T.; data curation, Y.Z.; writing—original draft preparation, R.K. and Y.Z.; writing—review and editing, K.S., Y.Z., I.Y. and M.T.; supervision, K.S. and M.T.; project administration, K. S. and M.T. All authors have read and agreed to the published version of the manuscript.

Funding: This research was funded by the Japan Society for the Promotion of Science (JSPS) KAKENHI (Grant-in-Aid for Challenging Exploratory Research, Grant 22K18916).

Institutional Review Board Statement: Not applicable.

Informed Consent Statement: Not applicable.

Data Availability Statement: Not applicable.

Acknowledgments: This study was partially supported by a grant from the Japan Society for the Promotion of Science (JSPS) KAKENHI (Grant-in-Aid for Challenging Exploratory Research, Grant 22K18916). Additionally, a portion of this work was supported by NIMS Electron Microscopy Analysis Station, Nanostructural Characterization Group. The authors also thank the Analysis and Instrumentation Center at the Nagaoka University of Technology for providing their facilities.

Conflicts of Interest: The authors declare no conflict of interest.

References

1. Lau, M.; Giri, K.; Garcia-Bennett, A.E. Antioxidant Properties of Probucol Released from Mesoporous Silica. *Eur. J. Pharm. Sci.* **2019**, *138*, 105038. [CrossRef] [PubMed]
2. Marchi, J.; Ussui, V.; Delfino, C.S.; Bressiani, A.H.A.; Marques, M.M. Analysis in Vitro of the Cytotoxicity of Potential Implant Materials. I: Zirconia-Titania Sintered Ceramics. *J. Biomed. Mater. Res. B. Appl. Biomater.* **2010**, *94*, 305–311. [CrossRef] [PubMed]
3. Tanaka, T.; Shimazu, R.; Nagai, H.; Tada, M.; Nakagawa, T.; Sandhu, A.; Handa, H.; Abe, M. Preparation of Spherical and Uniform-Sized Ferrite Nanoparticles with Diameters between 50 and 150 Nm for Biomedical Applications. *J. Magn. Magn. Mater.* **2009**, *321*, 1417–1420. [CrossRef]
4. Rosenholm, J.M.; Peuhu, E.; Eriksson, J.E.; Sahlgren, C.; Lindén, M. Targeted Intracellular Delivery of Hydrophobic Agents Using Mesoporous Hybrid Silica Nanoparticles as Carrier Systems. *Nano. Lett.* **2009**, *9*, 3308–3311. [CrossRef] [PubMed]
5. Kataoka, T.; Shiba, K.; Nagata, S.; Yamada, I.; Chai, Y.; Tagaya, M. Preparation of Monodispersed Nanoporous Eu(III)/Titania Loaded with Ibuprofen: Optimum Loading, Luminescence, and Sustained Release. *Inorg. Chem.* **2021**, *60*, 8765–8776. [CrossRef] [PubMed]
6. Chiavaioli, F.; Biswas, P.; Trono, C.; Jana, S.; Bandyopadhyay, S.; Basumallick, N.; Giannetti, A.; Tombelli, S.; Bera, S.; Mallick, A.; et al. Sol-Gel-Based Titania-Silica Thin Film Overlay for Long Period Fiber Grating-Based Biosensors. *Anal. Chem.* **2015**, *87*, 12024–12031. [CrossRef]
7. Arcos, D.; Vallet-Regí, M. Sol-Gel Silica-Based Biomaterials and Bone Tissue Regeneration. *Acta. Biomater.* **2010**, *6*, 2874–2888. [CrossRef]
8. Li, Z.; Hou, B.; Xu, Y.; Wu, D.; Sun, Y.; Hu, W.; Deng, F. Comparative Study of Sol-Gel-Hydrothermal and Sol-Gel Synthesis of Titania-Silica Composite Nanoparticles. *J. Solid. State. Chem.* **2005**, *178*, 1395–1405. [CrossRef]
9. Aw, M.S.; Addai-Mensah, J.; Losic, D. A Multi-Drug Delivery System with Sequential Release Using Titania Nanotube Arrays. *Chem. Comm.* **2012**, *48*, 3348–3350. [CrossRef]
10. Aw, M.S.; Losic, D. Ultrasound Enhanced Release of Therapeutics from Drug-Releasing Implants Based on Titania Nanotube Arrays. *Int. J. Pharm.* **2013**, *443*, 154–162. [CrossRef]
11. Kasar, S.; Kumar, S.; Kar, A.S.; Godbole, S.V.; Tomar, B.S. Sorption of Eu(III) by Amorphous Titania, Anatase and Rutile: Denticity Difference in Surface Complexes. *Col. Surf. A. Physicochem. Eng. Asp.* **2013**, *434*, 72–77. [CrossRef]
12. Ekka, B.; Sahu, M.K.; Patel, R.K.; Dash, P. Titania Coated Silica Nanocomposite Prepared via Encapsulation Method for the Degradation of Safranin-O Dye from Aqueous Solution: Optimization Using Statistical Design. *Water. Resour. Ind.* **2019**, *22*, 100071. [CrossRef]
13. Deng, Y.; Qi, D.; Deng, C.; Zhang, X.; Zhao, D. Superparamagnetic High-Magnetization Microspheres with an Fe_3O_4@SiO_2 Core and Perpendicularly Aligned Mesoporous SiO2 Shell for Removal of Microcystins. *J. Am. Chem. Soc.* **2008**, *130*, 28–29. [CrossRef] [PubMed]
14. Jana, N.R.; Earhart, C.; Ying, J.Y. Synthesis of Water-Soluble and Functionalized Nanoparticles by Silica Coating. *Chem. Mater.* **2007**, *19*, 5074–5082. [CrossRef]
15. Shiba, K.; Sato, S.; Ogawa, M. Preparation of Well-Defined Titania-Silica Spherical Particles. *J. Mater. Chem.* **2012**, *22*, 9963–9969. [CrossRef]
16. He, Q.; Shi, J.; Zhu, M.; Chen, Y.; Chen, F. The Three-Stage in Vitro Degradation Behavior of Mesoporous Silica in Simulated Body Fluid. *Microporous. Mesoporous. Mater.* **2010**, *131*, 314–320. [CrossRef]

17. Raula, J.; Eerikäinen, H.; Peltonen, L.; Hirvonen, J.; Kauppinen, E. Aerosol-Processed Polymeric Drug Nanoparticles for Sustained and Triggered Drug Release. *J. Control. Release* **2010**, *148*, e52–e53. [CrossRef]
18. Zhao, C.; Zhuang, X.; He, P.; Xiao, C.; He, C.; Sun, J.; Chen, X.; Jing, X. Synthesis of Biodegradable Thermo- and PH-Responsive Hydrogels for Controlled Drug Release. *Polymer* **2009**, *50*, 4308–4316. [CrossRef]
19. Paital, S.R.; Dahotre, N.B. Wettability and Kinetics of Hydroxyapatite Precipitation on a Laser-Textured Ca-P Bioceramic Coating. *Acta. Biomater.* **2009**, *5*, 2763–2772. [CrossRef]
20. Barfeie, A.; Wilson, J.; Rees, J. Implant Surface Characteristics and Their Effect on Osseointegration. *Br Dent J* **2015**, 218. [CrossRef]
21. Shadanbaz, S.; Dias, G.J. Calcium Phosphate Coatings on Magnesium Alloys for Biomedical Applications: A Review. *Acta. Biomater.* **2012**, *8*, 20–30. [CrossRef] [PubMed]
22. Liu, Y.; De Groot, K.; Hunziker, E.B. Osteoinductive Implants: The Mise-En-Scène for Drug-Bearing Biomimetic Coatings. *Ann. Biomed. Eng.* **2004**, *32*, 398–406. [CrossRef] [PubMed]
23. Wolke, J.G.C.; Van Der Waerden, J.P.C.M.; Schaeken, H.G.; Jansen, J.A. In Vivo Dissolution Behavior of Various RF Magnetron-Sputtered Ca-P Coatings on Roughened Titanium Implants. *Biomater.* **2003**, *24*, 2623–2629. [CrossRef] [PubMed]
24. Leeuwenburgh, S.; Wolke, J.; Schoonman, J.; Jansen, J. Electrostatic Spray Deposition (ESD) of Calcium Phosphate Coatings. *J. Biomed. Mater. Res. A* **2003**, *66*, 330–334. [CrossRef]
25. Radin, S.R.; Ducheyne, P. Plasma Spraying Induced Changes of Calcium Phosphate Ceramic Characteristics and the Effect on in Vitro Stability. *J. Mater. Sci. Mater. Med.* **1992**, *3*, 33–42. [CrossRef]
26. Shang, Y.; Yamada, S.; Chai, Y.; Tagaya, M. Synthesis of Spherical Phosphorus-Containing Mesoporous Silica for Improving Their Reaction Behavior in Simulated Body Fluid. *Key. Eng. Mater.* **2018**, *782 KEM*, 59–64. [CrossRef]
27. Kataoka, T.; Shiba, K.; Wang, L.Y.; Yamada, S.; Tagaya, M. Hybrid Preparation of Terbium(III)-Doped Mesoporous Silica Particles with Calcium Phosphates. *RSC Adv.* **2017**, *7*, 19479–19485. [CrossRef]
28. Lin, X.; De Groot, K.; Wang, D.; Hu, Q.; Wismeijer, D.; Liu, Y. A Review Paper on Biomimetic Calcium Phosphate Coatings. *Open Biomed. Eng. J.* **2015**, *9*, 56–64. [CrossRef]
29. Li, F.; Feng, Q.L.; Cui, F.Z.; Li, H.D.; Schubert, H. A Simple Biomimetic Method for Calcium Phosphate Coating. *Surf. Coat. Technol.* **2002**, *154*, 88–93. [CrossRef]
30. Leeuwenburgh, S.; Layrolle, P.; Barrre, F.; De Bruijn, J.; Schoonman, J.; Van Blitterswijk, C.A.; De Groot, K. Osteoclastic Resorption of Biomimetic Calcium Phosphate Coatings in Vitro. *J. Biomed. Mater. Res.* **2001**, *56*, 208–215. [CrossRef]
31. Cao, J.; Lian, R.; Jiang, X.; Liu, X. Formation of Porous Apatite Layer after Immersion in SBF of Fluorine-Hydroxyapatite Coatings by Pulsed Laser Deposition Improved in Vitro Cell Proliferation. *ACS. Appl. Bio. Mater.* **2020**, *3*, 3698–3706. [CrossRef]
32. Tanahashi, M.; Matsuda, T. Surface Functional Group Dependence on Apatite Formation on Self- Assembled Monolayers in a Simulated Body Fluid. *J. Biomed. Mater. Res.* **1997**, *34*, 305–315. [CrossRef]
33. Gu, Y.W.; Khor, K.A.; Cheang, P. In Vitro Studies of Plasma-Sprayed Hydroxyapatite/Ti-6Al-4V Composite Coatings in Simulated Body Fluid (SBF). *Biomater.* **2003**, *24*, 1603–1611. [CrossRef] [PubMed]
34. Cui, W.; Beniash, E.; Gawalt, E.; Xu, Z.; Sfeir, C. Biomimetic Coating of Magnesium Alloy for Enhanced Corrosion Resistance and Calcium Phosphate Deposition. *Acta. Biomater.* **2013**, *9*, 8650–8659. [CrossRef]
35. Bigi, A.; Boanini, E.; Bracci, B.; Facchini, A.; Panzavolta, S.; Segatti, F.; Sturba, L. Nanocrystalline Hydroxyapatite Coatings on Titanium: A New Fast Biomimetic Method. *Biomater.* **2005**, *26*, 4085–4089. [CrossRef] [PubMed]
36. Braun, K.; Pochert, A.; Beck, M.; Fiedler, R.; Gruber, J.; Lindén, M. Dissolution Kinetics of Mesoporous Silica Nanoparticles in Different Simulated Body Fluids. *J. Solgel. Sci. Technol.* **2016**, *79*, 319–327. [CrossRef]
37. Chai, Y.; Maruko, Y.; Liu, Z.; Tagaya, M. Design of Oriented Mesoporous Silica Films for Guiding Protein Adsorption States. *J. Mater. Chem. B.* **2021**, *9*, 2054–2065. [CrossRef]
38. Kim, S.R.; Lee, J.H.; Kim, Y.T.; Riu, D.H.; Jung, S.J.; Lee, Y.J.; Chung, S.C.; Kim, Y.H. Synthesis of Si, Mg Substituted Hydroxyapatites and Their Sintering Behaviors. *Biomaterials* **2003**, *24*, 1389–1398. [CrossRef]
39. Eliad, L.; Salitra, G.; Soffer, A.; Aurbach, D. Ion Sieving Effects in the Electrical Double Layer of Porous Carbon Electrodes: Estimating Effective Ion Size in Electrolytic Solutions. *J. Phy. Chem. B.* **2001**, *105*, 6880–6887. [CrossRef]
40. Banda, H.; Daffos, B.; Périé, S.; Chenavier, Y.; Dubois, L.; Aradilla, D.; Pouget, S.; Simon, P.; Crosnier, O.; Taberna, P.L.; et al. Ion Sieving Effects in Chemically Tuned Pillared Graphene Materials for Electrochemical Capacitors. *Chem. Mater.* **2018**, *30*, 3040–3047. [CrossRef]
41. Porter, D.W.; Wu, N.; Hubbs, A.F.; Mercer, R.R.; Funk, K.; Meng, F.; Li, J.; Wolfarth, M.G.; Battelli, L.; Friend, S.; et al. Differential Mouse Pulmonary Dose and Time Course Responses to Titanium Dioxide Nanospheres and Nanobelts. *Toxicol. Sci.* **2013**, *131*, 179–193. [CrossRef]
42. Oberdorster, G.; Ferin, J.; Gelein, R.; Soderholm, S.C.; Finkelstein, J. Role of the Alveolar Macrophage in Lung Injury: Studies with Ultrafine Particles. *Environ. Health Perspect.* **1992**, *97*, 193–199. [PubMed]
43. Yu, J.C.; Zhang, L.; Zheng, Z.; Zhao, J. Synthesis and Characterization of Phosphated Mesoporous Titanium Dioxide with High Photocatalytic Activity. *Chem. Mater.* **2003**, *15*, 2280–2286. [CrossRef]
44. Huang, X.; Wang, P.; Yin, G.; Zhang, S.; Zhao, W.; Wang, D.; Bi, Q.; Huang, F. Removal of Volatile Organic Compounds Driven by Platinum Supported on Amorphous Phosphated Titanium Oxide. *Wuji Cailiao Xuebao/J. Inorg. Mater.* **2020**, *35*, 482–490.
45. Aizawa, M.; Nosaka, Y.; Fujii, N. FT-IR Liquid Attenuated Total Reflection Study of TiO_2-SiO_2 Sol-Gel Reaction. *J. Non-Cryst. Solids* **1991**, *128*, 77–85. [CrossRef]

46. Schraml, M.; Walther, K.; Wokaun, A.; Handy, B.; Baiker, A. Porous Silica Gels and TiO_2/SiO_2 Mixed Oxides Prepared via the Sol-Gel Process: Characterization by Spectroscopic Techniques. *J. Non-Cryst. Solids* **1992**, *143*, 93–111. [CrossRef]
47. Thommes, M.; Kaneko, K.; Neimark, A.; Olivier, J.P.; Rodriguez-Reinoso, F.; Rouquerol, J.; Sing, K.S.W. Physisorption of Gases, with Special Reference to the Evaluation of Surface Area and Pore Size Distribution (IUPAC Technical Report). *Pure. Appl. Chem.* **2015**, *87*, 1051–1069. [CrossRef]
48. Kokubo, T.; Kushitani, H.; Sakka, S.; Kitsugi, T.; Yamamuro, T. Solutions Able to Reproduce in Vivo Surface-Structure Changes in Bioactive Glass-Ceramic A-W3. *J. Biomed. Mater. Res.* **1990**, *24*, 721–734. [CrossRef] [PubMed]
49. Atkinson, D.; McLeod, A.I.; Sing, K.S.W. Adsorptive Properties of Microporous Carbons: Primary and Secondary Micropore Filling. *J. Chim. Phys.* **1984**, *81*, 791–794. [CrossRef]
50. Mikhail, R.S.; Brunauer, S.; Bodor, E.E. Investigations of a Complete Pore Structure Analysis I. *Anal. Micropores; J. coll. Interf Sci.* **1968**, *26*, 45–53. [CrossRef]
51. Setoyama, N.; Suzuki, T.; Kaneko, K. A Molecular Simulation Study on Empirical Determination Method of Pore Structures of Activated Carbons. *Tanso* **1997**, *1997*, 159–166. [CrossRef]